

Adsorption of Organic Molecules on Kaolinite from the Exchange-Hole Dipole Moment Dispersion Model

Erin R. Johnson* and Alberto Otero-de-la-Roza*

Chemistry and Chemical Biology, School of Natural Sciences, University of California, Merced, 5200 North Lake Road, Merced, California 95343, United States

ABSTRACT: Intermolecular interactions between organic molecules and clay minerals are important in a wide range of chemical applications, ranging from oil-sands petroleum extraction to environmental chemistry and catalysis. The binding energies between each of benzene, *n*-hexane, pyridine, 2-propanol, and water and the kaolinite surface are calculated using density functional theory with the exchange-hole dipole moment dispersion model. The dominant noncovalent interactions are found to be hydrogen bonding for pyridine, 2-propanol, and water, OH- π interactions for benzene, and CH-O interactions for *n*-hexane. All molecules considered are more strongly bound to the hydrophilic alumina face, rather than the hydrophobic siloxane face, of kaolinite.

1. INTRODUCTION

Clay minerals, such as kaolinite, find industrial applications in water purification, remediation of soil contamination, and heterogeneous catalysis¹ because of their high binding affinities toward a diversity of chemical species. However, the high binding affinity is also a key challenge in extraction of bitumen from oil sands for petroleum production, because much of the extracted bitumen remains attached to minute clay particles.^{2–4} The chemical nature of these intermolecular interactions is not fully understood and is the subject of ongoing research.^{5–7}

Kaolinite,^{8,9} a common clay found in oil sands, has the chemical formula $\text{Al}_2\text{Si}_2\text{O}_5(\text{OH})_4$. It is composed of a series of uncharged layers connected by a network of hydrogen bonds, as shown in Figure 1. The individual layers are formed by two sheets, one consisting of SiO_4 tetrahedra and one consisting of

AlO_6 octahedra, which are connected via bonding to the oxygen atoms. The octahedral surface is terminated by hydroxyl groups, which form hydrogen bonds to the siloxyl oxygen atoms of the adjacent layer. Previous theoretical work showed that water binds strongly to the octahedral alumina surface (14.7 kcal/mol) and weakly to the tetrahedral siloxane surface (4.1 kcal/mol).¹⁰ Water and 2-isopropanol present almost the same binding energies on both sides of kaolinite, with similar dispersion effects, pointing toward the dominant effect of the hydrogen bond on the overall binding.

There have been relatively few theoretical studies of the intermolecular interactions responsible for binding of organic molecules to clay surfaces. Previous studies focused on possible soil contaminants, such as formamide, N-methyl-formamide, and dimethylsulfoxide,¹¹ benzene,¹² thiophene,¹³ dioxins,¹⁴ phenoxyacetic acid,¹⁵ and 1,3,5-trinitrobenzene.^{16,17} Additional works considered sarin and soman¹⁸ for disposal of nerve gases, and thymine and uracil DNA bases¹⁹ for catalytic assembly of bioorganic molecules. With the single exception of cluster calculations on trinitrobenzene using the MP2 method,¹⁷ these studies used conventional density functional theory (DFT) calculations, which fail to capture the correct physics of London dispersion interactions.²⁰

Dispersion is the weakest of the van der Waals interactions, arising when an instantaneous dipole in the charge distribution of one atom or molecule induces an instantaneous dipole in a nearby atom or molecule. Dispersion is the principal intermolecular interaction between nonpolar species and also plays an important role in physisorption of molecules on surfaces. Previous computational studies have shown that dispersion contributes as much as half of the adsorption energy between trinitrobenzene and kaolinite.^{16,17} Dispersion was further demonstrated to be important for adhesion of kaolinite layers, contributing approximately one third of the interaction

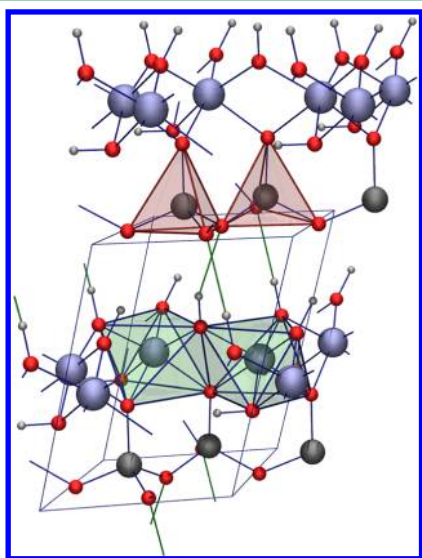


Figure 1. Structure of bulk kaolinite, displaying the octahedral alumina and tetrahedral siloxane layers. Interlayer hydrogen bonds are marked in green. Color key: red (O), white (H), lilac (Al), and gray (Si).

Special Issue: Berny Schlegel Festschrift

Received: July 23, 2012

Published: September 11, 2012

energy, even though this is formally considered to be hydrogen bonding.⁹ Therefore, a physically reasonable treatment of dispersion will be essential in theoretical studies of molecular adsorption to kaolinite clay.

In this work, density functional theory (DFT) and the exchange-hole dipole moment (XDM) dispersion model^{21,22} are used to study binding of four small organic molecules (benzene, *n*-hexane, pyridine, and 2-propanol) with both alumina and siloxane surfaces of kaolinite. The XDM method is further applied to calculate potential energy surfaces for diffusion of benzene along both kaolinite surfaces. The noncovalent interactions (NCI)^{23–25} index is used to identify key interactions between the organic molecules and the clay.

2. THEORY

2.1. XDM Dispersion Model. The exchange-hole dipole moment (XDM) method developed by Becke and Johnson is a DFT-based approach to model dispersion.²¹ The XDM dispersion energy is obtained from second-order perturbation theory within the closure approximation.²⁶ The basis of the approach is that the instantaneous dipole moments responsible for dispersion attraction are modeled using the dipole moment of the exchange hole. The resulting dispersion energy is then added to the DFT energy in a post-SCF fashion.

$$E = E_{\text{DFT}} + E_{\text{disp}} \quad (1)$$

The dispersion energy contains the first three terms in the series expansion and involves a sum over all pairs of atoms *i* and *j*.

$$E_{\text{disp}} = - \sum_{n=6,8,10} \sum_{i < j} \frac{C_{n,ij}}{R_{ij}^n + R_{\text{vdW},ij}^n} \quad (2)$$

In this equation, the dispersion energy is damped using the interatomic van der Waals radii $R_{\text{vdW},ij}$ to prevent divergence at small interatomic separations R_{ij} .

The dispersion coefficients C_6 , C_8 , and C_{10} are calculated from first-principles quantities as follows:

$$C_{6,ij} = \frac{\alpha_i \alpha_j \langle M_1^2 \rangle_i \langle M_1^2 \rangle_j}{\alpha_i \langle M_1^2 \rangle_j + \alpha_j \langle M_1^2 \rangle_i} \quad (3)$$

$$C_{8,ij} = \frac{3}{2} \frac{\alpha_i \alpha_j (\langle M_1^2 \rangle_i \langle M_2^2 \rangle_j + \langle M_2^2 \rangle_i \langle M_1^2 \rangle_j)}{\alpha_i \langle M_1^2 \rangle_j + \alpha_j \langle M_1^2 \rangle_i} \quad (4)$$

$$C_{10,ij} = 2 \frac{\alpha_i \alpha_j (\langle M_1^2 \rangle_i \langle M_3^2 \rangle_j + \langle M_3^2 \rangle_i \langle M_1^2 \rangle_j)}{\alpha_i \langle M_1^2 \rangle_j + \alpha_j \langle M_1^2 \rangle_i} + \frac{21}{5} \frac{\alpha_i \alpha_j \langle M_2^2 \rangle_i \langle M_2^2 \rangle_j}{\alpha_i \langle M_1^2 \rangle_j + \alpha_j \langle M_1^2 \rangle_i} \quad (5)$$

The α 's are atom-in-molecule polarizabilities obtained by scaling the free atomic values using a ratio of Hirshfeld atomic volumes.²⁷ The $\langle M_l^2 \rangle$ are the expectation values of the squared *l*-pole moments of the exchange hole, projected onto atomic regions using Hirshfeld partitioning weights, w_i ,

$$\langle M_l^2 \rangle_i = \sum_{\sigma} \int w_i(\mathbf{r}) \rho_{\sigma}(\mathbf{r}) [r_i^l - (r_i - d_{X\sigma})^l]^2 d\mathbf{r} \quad (6)$$

where ρ_{σ} is the spin density, r_i is the distance from nucleus *i*, and $d_{X\sigma}$ is the magnitude of the exchange-hole dipole moment.

While the original XDM formulation used the exact (Hartree–Fock) exchange hole dipole moment, this is quite computationally demanding for periodic systems using a plane-wave basis set. A more efficient, and somewhat more accurate,^{28,29} alternative is to use the Becke–Roussel (BR)³⁰ model of the exchange hole. The BR functional uses only local density-based quantities (the density, ρ , its gradient, $\nabla\rho$, Laplacian, $\nabla^2\rho$, and the kinetic energy density, τ) to model the exchange hole and calculation of the dispersion correction is a negligible addition to the total computational cost. In this work, the BR variant of the XDM model is used throughout.

While the XDM dispersion coefficients are nonempirical, two (universal) parameters are introduced to define the van der Waals radii used in the damping function.

$$R_{\text{vdW},ij} = \frac{a_1}{3} \left[\left(\frac{C_{8,ij}}{C_{6,ij}} \right)^{1/2} + \left(\frac{C_{10,ij}}{C_{8,ij}} \right)^{1/2} + \left(\frac{C_{10,ij}}{C_{6,ij}} \right)^{1/4} \right] + a_2 \quad (7)$$

The optimum parameter values for use with the B86bPBE^{31,32} density functional are $a_1 = 0.136$ and $a_2 = 3.178$ Å. These values were obtained in our previous work by minimizing the root-mean-square percent error for a set of 65 intermolecular binding energies.²²

In addition to its success for molecular dimers ranging from noble gases to DNA bases,²⁹ the XDM model was recently benchmarked for periodic solids. It was found to give excellent results for the exfoliation energy of graphite²² and structures and energetics of molecular crystals.³³ Additionally, XDM almost doubled the accuracy of other dispersion-corrected DFT methods for a set of 21 sublimation enthalpies,³³ correcting the systematic overbinding present in other popular dispersion-including functionals.

2.2. NCI Index. The recently developed noncovalent interactions (NCI) index provides a simple approach to visualize both intra- and intermolecular interactions in real space.^{23–25} The NCI method depends exclusively on the electron density and its reduced gradient *s*:

$$s = \frac{1}{2(3\pi^2)^{1/3}} \frac{|\nabla\rho|}{\rho^{4/3}} \quad (8)$$

Plots of *s* versus ρ have a characteristic stiletto-heel shape that allows identification of noncovalent interactions as regions with both low density and low reduced gradient. In real space, noncovalent interactions are visualized by plotting low *s* isosurfaces, subject to an additional low density constraint. The NCI regions are able to map the noncovalent interactions indirectly, by revealing the real space loci where closed-shell fragments experience mutual Pauli repulsion.²⁵

Interactions can additionally be classified as attractive or repulsive according to the sign of the second density Hessian eigenvalue (λ_2). This distinguishes between bonding ($\lambda_2 < 0$) and nonbonding ($\lambda_2 > 0$) interactions, depending on whether the electron density is locally accumulated or depleted with respect to the plane normal to the bond path. Qualitatively, the interaction strength also is related to the density values, so NCI isosurfaces are colored according to the value of $\text{sign}(\lambda_2)\rho$. These surfaces can be computed rapidly, even for large molecules or periodic solids.

3. COMPUTATIONAL DETAILS

All results reported in this work were obtained using the PAW method³⁴ in a plane-wave basis set, as implemented in the Quantum-ESPRESSO package.³⁵ A combination of the B86b exchange functional³¹ with PBE correlation³² was used together with the exchange-hole dipole moment model (XDM)²² to incorporate dispersion effects. The calculations in the bulk were carried out using the following parameters: 50 Ry plane-wave kinetic energy cutoff, 300 Ry density cutoff, and a $4 \times 4 \times 2$ regular k -point grid. The convergence of the total energy with these parameters is on the order of ≈ 1 mRy.

The surfaces were simulated by taking a 2×2 supercell, cleaving the (001) hydrogen-bond surface and stretching the c direction of the crystal to incorporate a vacuum 25 Å long. The calculation parameters used are the same as in the bulk, except for the k -point grid ($2 \times 2 \times 1$). A single point at Γ was used in the calculation of the isolated molecules, which were simulated using supercells with a c -parameter length of 25 (benzene), 35 (pyridine), 35 (2-propanol), 35 (hexane), and 25 Å (water).

4. RESULTS

We first validate the B86bPBE-XDM approach for the structure of bulk kaolinite. Computed geometric parameters are shown in Table 1 along with literature values from a previous study⁹

Table 1. Geometric Parameters Describing Bulk Kaolinite Calculated Using B86bPBE, with and without XDM Dispersion^a

param.	B86bPBE	B86bPBE-XDM	B3LYP	B3LYP-D*	exp.
a	5.236	5.185	5.230	5.184	5.17
b	5.220	5.171	5.210	5.190	5.15
c	7.523	7.344	7.480	7.396	7.39
α	59.9	59.9	59.9	59.9	59.9
β	99.0	98.9	98.8	99.8	99.1
γ	84.1	84.0	84.1	83.5	84.2
volume	171.7	164.4	170.3	165.0	164.3

^aPrevious literature results⁹ and the experimental crystal structure³⁹ are given for comparison.

using B3LYP^{36,37} with a modified version of Grimme's DFT-D dispersion correction.³⁸ The B86bPBE-XDM results are in good agreement with both B3LYP-D* and the experimental crystal structure.³⁹ As noted previously, inclusion of dispersion leads to greater interlayer attraction. The largest difference in results between conventional and dispersion-corrected functionals occurs for the interlayer direction, c , where inclusion of dispersion gives better agreement with experiment.

Computed B86bPBE-XDM binding energies for selected orientations of benzene, n -hexane, pyridine, 2-propanol, and water on both siloxane and alumina surfaces of kaolinite are collected in Table 2. All of the organic molecules show stronger binding to the more hydrophilic alumina face. The binding energies follow the trend benzene \approx n -hexane < pyridine < 2-propanol < water, as would be expected from their polarity and previous experimental results.⁵ In the particular case of n -hexane, several conformations can be considered. We explored both a linear (as shown in Figure 4) and a folded conformation. The difference in binding energies to both surfaces is on the order of ≈ 1 kcal/mol, so for simplicity we are going to consider only the linear conformation.

Table 2. Binding Energies on the Kaolinite (001) Surface (kcal/mol of Adsorbed Molecules)^a

molecule	surface	orientation	B86bPBE-XDM	no E_{disp}
benzene	siloxane	parallel	7.6	-2.8
	siloxane	perpend.	5.4	-1.0
	alumina	parallel	11.4	0.4
	alumina	perpend.	6.2	1.0
n -hexane	siloxane	parallel	8.9	-2.2
	alumina	parallel	11.6	-1.2
pyridine	siloxane	perpend.	12.7	1.1
	siloxane	parallel	11.9	-0.4
	alumina	perpend.	15.9	7.8
2-propanol	alumina	parallel	14.9	3.6
	siloxane	donor	8.3	1.2
	alumina	donor	17.0	10.5
water	alumina	acceptor	15.2	6.6
	siloxane	donor	8.1	2.2
	alumina	donor	18.3	12.4
	alumina	acceptor	17.4	11.5

^aGeometry optimizations were performed using B86bPBE-XDM. Energies are also reported without the dispersion term at the converged B86bPBE-XDM geometry.

Table 2 also reports binding energies obtained at the same B86bPBE-XDM optimized geometries, but without including the dispersion term. This allows the relative importance of the dispersion contribution to the binding energy to be assessed. We find that dispersion is responsible for virtually all of the binding, with the exceptions of pyridine, 2-propanol, and water on the alumina face. In these cases, the binding energies without dispersion range from 6.6 to 12.4 kcal/mol, which can be attributed to hydrogen bonds between the substrate and the surface. Reoptimization of the geometry using the uncorrected B86bPBE increases the binding energy by a few kcal/mol. For instance, upon geometry relaxation without XDM, the binding energy of benzene to the siloxane and alumina surfaces is 0.1 and 1.3 kcal/mol in the parallel orientation and 0.7 and 1.0 kcal/mol in the perpendicular orientation, respectively, to be compared to the values reported in Table 2. The dispersion energy is, in any case, essential in the description of the adsorption.

The results in Table 2 for benzene are compatible with the adsorption energies reported by Rimola et al.⁴⁰ In this work, the adsorption of benzene on kaolinite-like surfaces was calculated using dispersion-corrected B3LYP in a Gaussian basis set. The authors report a binding energy in the range 7.6 to 11.0 kcal/mol for the adsorption of benzene on the siloxane-like surface, the variability coming from the different methods employed and the inclusion or lack of basis set superposition error (BSSE) corrections. On the alumina surface, the authors found the binding energies to range between 11.6 and 16.4 kcal/mol. These values are consistent with Table 2: the adsorption is stronger on the alumina surface, and the agreement of our data (7.6 and 11.4 kcal/mol on siloxane and alumina surfaces) is quantitatively comparable to the corresponding BSSE-corrected B3LYP-D* values (7.6 and 11.6 kcal/mol).

For comparison with previous studies, we calculated the binding energy of water to both surfaces, as shown in Table 2. Our results are consistent with Tunega et al.¹⁰ in predicting that the binding to the alumina is much stronger than to the siloxane surface. The B86b-XDM values are also consistent with the ones recently reported by Tosoni et al.⁴¹ for silica surfaces

(11.5 and 13.4 kcal/mol depending on whether or not the BSSE correction is included), which closely resemble the alumina surface in kaolinite.

5. DISCUSSION

5.1. Benzene. The most stable arrangements for benzene on both kaolinite surfaces are shown in Figure 2 together with

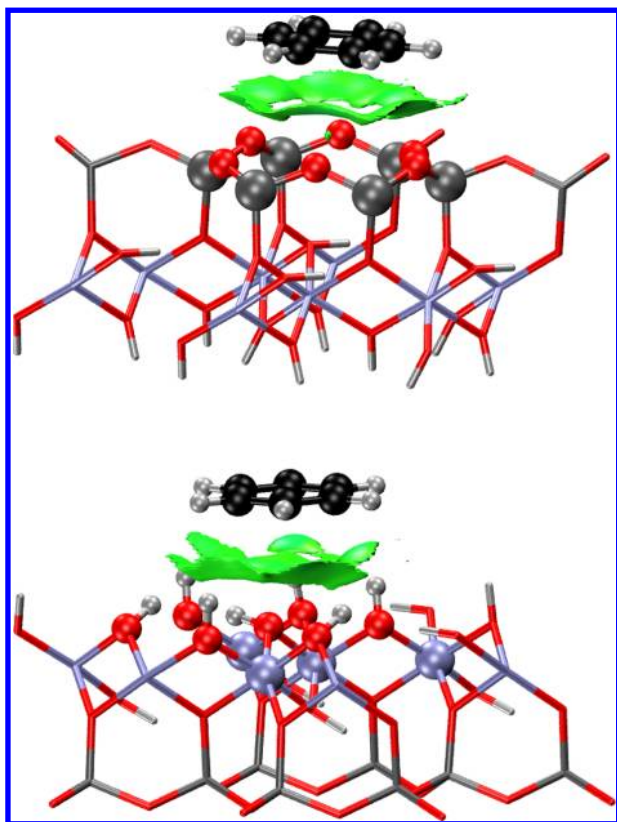


Figure 2. NCI plots ($s = 0.7$ au) of benzene on the kaolinite surface. On the siloxane surface (top), the distances between the surface oxygens and the benzene hydrogens are in the range 3.2 to 3.5 Å. The center of mass of the benzene is 3.1 Å above the plane of oxygens. On the alumina surface, two close surface hydrogen–carbon contacts appear at 2.5 and 2.6 Å. The center of mass is 3.4 Å above an oxygen. The center of mass distance to the surface increases to 4.1 Å (siloxane) and 3.8 Å (alumina) when the geometry is optimized without the XDM correction.

calculated NCI isosurfaces. The NCI approach allows identification of the key noncovalent interactions responsible for binding between the substrate and surface. This analysis indicates whether the interactions are localized to a few atoms or are spread more evenly over the adjacent faces of the organic molecules and kaolinite surface.

It is found that benzene prefers to lie flat on the alumina face, forming OH– π interactions with several of the surface OH groups. This type of interaction was already proposed for binding of benzene to clay surfaces in the literature.⁷ Experimental results for adsorption of a pentane-insoluble bitumen fraction (primarily composed of polyaromatic molecules with associated polar groups) on kaolinite⁵ also support our finding of OH– π interactions. IR absorbance peaks at 3626 cm^{-1} and 3696 cm^{-1} were assigned to OH stretching modes for hydroxyl groups located within the volume of the layer and surface hydroxyl groups, respectively. Adsorption of

organic molecules was found to shift the peak at 3696 to 3683 cm^{-1} , and this shift was attributed to interactions between kaolinite surface OH groups and the organic species.⁵

Our calculations show that benzene also binds favorably to the siloxane surface via dispersion interactions. Figure 2 shows that the benzene CH bonds align toward oxygen lone pairs and the center of the benzene ring lies over a tetrahedral hole. However, binding to the siloxane face is weaker than to the alumina face by 3.9 kcal/mol.

T-shaped arrangements, in which the benzene C–H bonds interact with the surface oxygen atoms, are possible on both surfaces, but they are substantially less stable than the parallel orientation. These findings are in agreement with previous simulations of thiophene¹³ and phenoxyacetic acid herbicides¹⁵ on the octahedral surface of kaolinite, which showed that the aromatic rings lay essentially flat along the surface, even using GGA functionals that neglect dispersion. Additionally, experiments on adsorption of benzyl alcohol on kaolinite indicate that the available area per molecule is sufficient for the alcohol to be adsorbed in an orientation with the benzene ring lying in the plane of the surface.⁴²

In all cases examined, the geometric distortion of the benzene molecule upon adsorption is negligible, pointing to a purely dispersion-dominated physisorption process. To evaluate the degree of molecule surface charge transfer, we calculated the Bader charges^{43,44} on all the systems examined. The charge of the benzene is in all cases less than 0.1 electrons, within the error of the Bader basin integration.

We additionally calculated potential energy surfaces (PES) for benzene migration, parallel to the surface, over both kaolinite faces. The PES are shown in Figure 3 and were generated by moving the benzene molecule over the surface in a uniform (x,y) grid. The center-of-mass position of the benzene was kept fixed relative to the surface, while the z -position (height above the surface) was allowed to relax.

On the alumina surface, the minimum-energy points on the PES (shown in purple) have the benzene center-of-mass lying almost directly over one of the upward-pointing surface O–H groups, again indicating that OH– π is the dominant non-covalent interaction. The maximum-energy points have the benzene center-of-mass lying over an OH group that is already participating in an internal hydrogen bond within the surface and not able to form a stabilizing OH– π interaction with the ring. The PES is fairly rough, with the energy scale ranging from 9 to 13 kcal/mol. On the siloxane surface, the minimum-energy points are somewhat off-center from the tetrahedral hole, to maximize CH–O interactions, while simultaneously minimizing contacts between the oxygen lone pairs and the benzene– π system. On this face, the PES is quite flat, spanning an energy range from 6.8 to 8.2 kcal/mol, so diffusion over the surface will be facile.

While binding of benzene to kaolinite is a relatively strong noncovalent interaction, we would still expect this binding to be reversible, as found experimentally for anthracene binding.⁴⁵ We would not expect these dispersion interactions to be a major impediment for separation of hydrocarbons from clays, and more complex, cooperative effects are likely responsible. Indeed, it is found that it is much more difficult to remove phenanthrene from wet clays.⁴⁶ Additionally, anthracene binding was found to dramatically increase when the clay surfaces were coated with highly-polar phthalate but not with more highly-substituted benzene carboxylic acids.⁴⁵ Oil-sands studies show that bitumen extraction is complicated by the

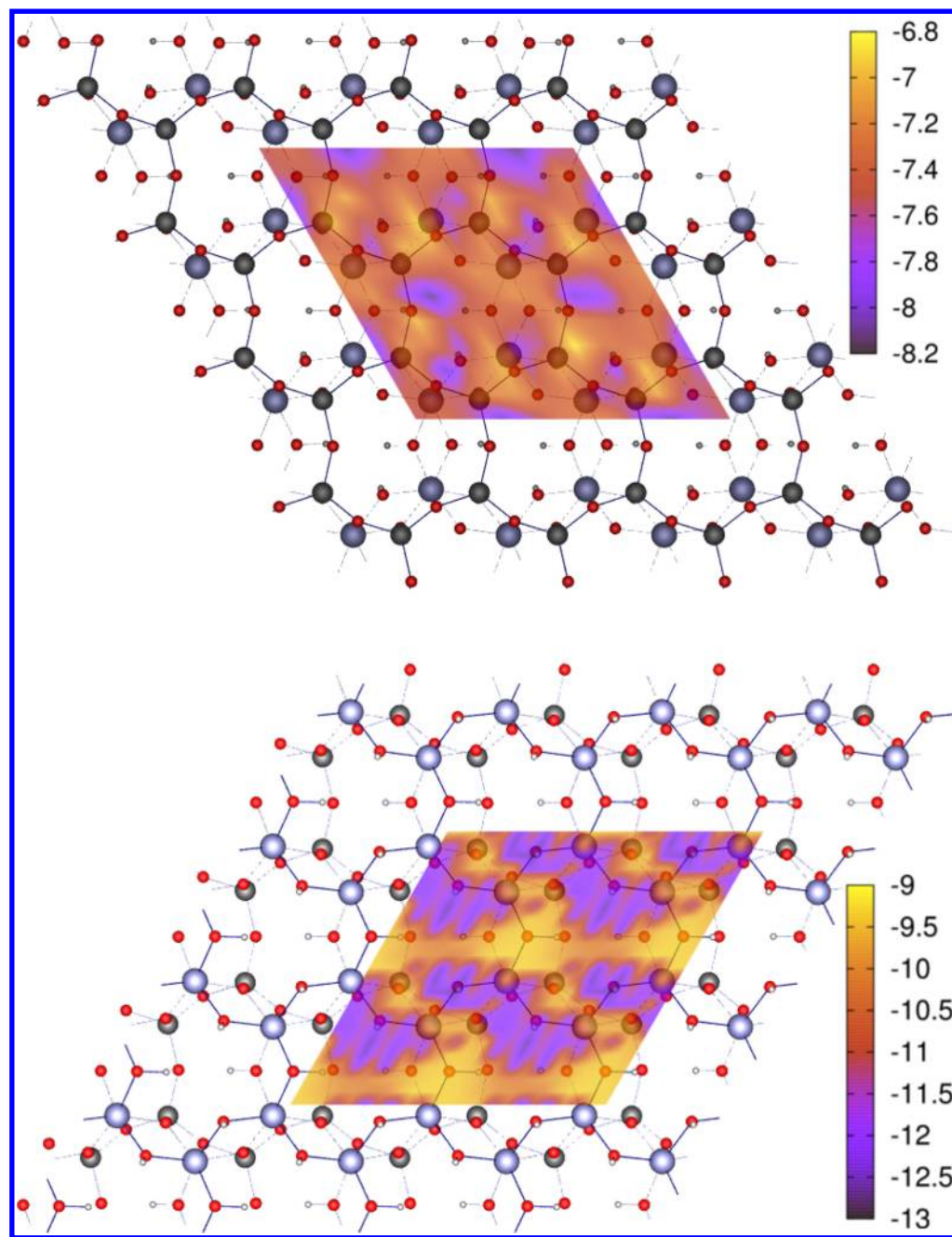


Figure 3. Potential energy surfaces for benzene migration over the siloxane and alumina faces of kaolinite. Units are kcal/mol. The atomic color scheme is the same as in Figure 1.

presence of divalent cations,^{6,7} which can form very strong cation- π interactions, on the order of covalent bond strengths.⁴⁷

5.2. Other Organic Molecules. NCI plots for the most stable arrangements of *n*-hexane, pyridine, 2-propanol, and water on both kaolinite faces are shown in Figure 4. For *n*-hexane, binding to the alumina surface is more favorable than to the siloxane surface by 2.7 kcal/mol. In both cases, the principal interactions are CH-O interactions with the C-H bonds pointing down toward the surface. This is particularly notable on the alumina surface, where two C-H bonds lie centered over the octahedral holes and are surrounded by surface oxygen atoms. These CH-O interactions are fairly strong, since the binding energy of *n*-hexane is approximately

equal to that of benzene on the alumina surface and 1.3 kcal/mol greater than benzene on the siloxane surface. Similar CH-O interactions are seen in molecular crystals.^{48,49}

For pyridine on the alumina face, two configurations are possible, with surface hydroxyl groups acting as a hydrogen-bond donors in both cases. If the pyridine is oriented perpendicular to the surface, the hydrogen bonding alignment is more favorable, but the pyridine can also lie parallel the surface, maximizing dispersion. The perpendicular arrangement is found to be more stable by 1 kcal/mol and the OH-N hydrogen bond can be clearly seen from the NCI plot in Figure 4. On the siloxane surface, the nitrogen experiences nonbonded repulsion from the oxygen lone pairs, so the pyridine molecule prefers to lie perpendicular to the surface, with the CH

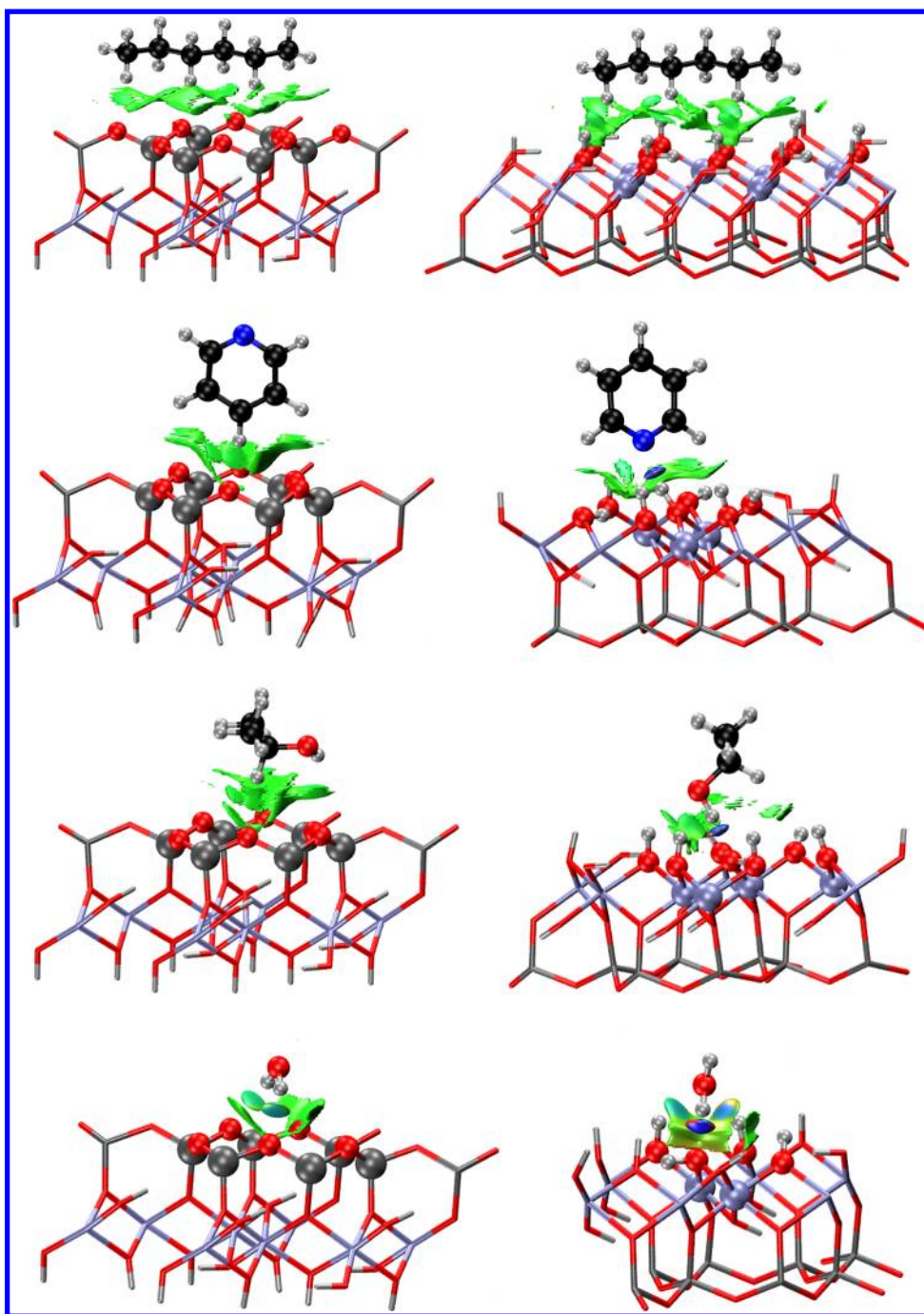


Figure 4. NCI plots ($s = 0.7$ au) of *n*-hexane (first row), pyridine (second), 2-propanol (third), and water (fourth row) on the siloxane (left) and alumina (right) surfaces. Color scheme: red (O), blue (N), white (H), lilac (Al), gray (Si), and black (C).

opposite to the nitrogen directly over the tetrahedral hole. The binding energy of pyridine in this orientation is 5.1 kcal/mol stronger than for benzene, presumably because of the favorable interaction between the permanent dipole of pyridine and the surface.

From Table 2, isopropanol is bound over twice as strongly to the alumina face than the siloxane face, and the binding energy of 17 kcal/mol is the largest obtained for the four organic molecules. The arrangement in which propanol acts a hydrogen-bond donor is 1.8 kcal/mol more stable than the case where propanol accepts a hydrogen bond from the alumina surface. On the siloxane face, propanol surprisingly does not prefer to form a hydrogen bond to one of the surface oxygen

atoms. Instead, the most stable configuration involves the central C–H bond pointing directly toward the tetrahedral hole of the surface to maximize CH–O interactions, as seen for pyridine and *n*-hexane. The NCI plots in 5.2 clearly reveal the CH–O interactions and OH–O hydrogen bonds for the siloxane and alumina faces, respectively. The case of water is similar to isopropanol: the binding is over twice as strong to the alumina face than to the siloxane face. The two possible orientations of water on the alumina face (donor and acceptor) are close in energy, with the donor conformation being slightly more stable. In the NCI plots for water, the hydrogen bonds appear as localized round high density (blue) regions. Our NCI results qualitatively agree with our XDM binding energies and

indicate that, as expected, pyridine, 2-propanol, and water are more strongly bound to kaolinite than either benzene or *n*-hexane.

Regarding intermolecular distances in Figure 4, *n*-hexane presents close CH–O distances with hydrogen–oxygen distances equal to 3.0 Å (siloxane) and 2.7 Å (alumina). In the case of pyridine on the alumina surface, the nitrogen is clearly participating a hydrogen bond, at a distance of 1.8 Å from the surface hydrogen. On the siloxane surface the hydrogen pointing toward the surface is approximately equidistant to three nearby oxygens, at a distance of 2.8 Å. A very similar distance and orientation is obtained for the tertiary carbon hydrogen in 2-propanol adsorbed to the siloxane side. The hydrogen bond, in this case, is avoided, with $d(\text{OH}–\text{O}) = 2.7$ Å. When this molecule adsorbs to the other face, however, a hydrogen bond is formed at a distance of 1.7 Å.

As in the case of benzene, the intramolecular distances are unaffected by the adsorption on either of the two surfaces, even when a CH–O interaction appears in the NCI plots. Only in the adsorption of 2-propanol via strong hydrogen bonding to the surface is the effect noticeable, with the intramolecular OH bond stretching from 0.97 Å to 1.00 Å. The calculated charge transfer between molecule and surface is, as in the case of benzene, less than 0.1 electrons in every case.

6. SUMMARY

In this article, we have examined the binding properties of several small organic molecules on kaolinite clay surfaces. This study gives relevant information on which to build an understanding of liquid adsorption on clay and its relevance for oil sands processing. To achieve this, we have employed a combination of first-principles density-functional theory (DFT) calculations under periodic boundary conditions and the noncovalent interactions (NCI) index, to probe the molecular adsorption to kaolinite surfaces.

The molecules studied were benzene, *n*-hexane, pyridine, 2-propanol, and water. We found that, as expected, dispersion interactions are essential in describing the physisorption energetics, particularly for the nonpolar molecules (benzene and *n*-hexane). In these, binding to the alumina surface (where O–H groups are available) proceeds through OH– π interactions with benzene and CH–O and OH–C interactions with the aliphatic chain in *n*-hexane. These binding modes are in agreement with previous experimental observations and theoretical simulations. Thanks to this binding mechanism, adsorption to the alumina surface is stronger than to the siloxane surface. Polar molecules (pyridine and 2-propanol) tend to form strong hydrogen bonds with the alumina surface whereas the adsorption to the siloxane side is similar to the nonpolar hydrocarbons.

In addition, the potential energy surface of benzene lying flat on both surfaces (the preferred orientation) has been mapped out, revealing that binding is stronger and transition barriers for minima hopping are higher on the alumina than on the siloxane side of a kaolinite surface. We expect this study to be a first step in the direction of understanding and improving industrial processes of bitumen extraction from oil sands.

AUTHOR INFORMATION

Corresponding Author

*E-mail: ejohnson29@ucmerced.edu; aoterodelaroza@ucmerced.edu.

Notes

The authors declare no competing financial interest.

ACKNOWLEDGMENTS

The authors acknowledge Dr. Gino A. DiLabio for helpful discussions and Han Bao for performing some preliminary calculations. A.O.R. thanks the Spanish Malta/Consolider initiative (No. CSD2007-00045).

REFERENCES

- (1) Murray, H. H. *Appl. Clay Sci.* **2000**, *17*, 207–221.
- (2) Masliyah, J.; Zhou, Z.; Xu, Z.; Czarnecki, J.; Hamza, H. *Can. J. Chem. Eng.* **2004**, *82*, 628–654.
- (3) Painter, P.; Williams, P.; Mannebach, E. *Energy Fuels* **2010**, *24*, 1094–1098.
- (4) Williams, P.; Lupinsky, A.; Painter, P. *Energy Fuels* **2010**, *24*, 2172–2173.
- (5) Tu, Y.; Kingston, D.; Kung, J.; Kotlyar, L. S.; Sparks, B. D.; Chung, K. H. *Pet. Sci. Technol.* **2006**, *24*, 327–338.
- (6) Liu, J.; Xu, Z.; Masliyah, J. *Can. J. Chem. Eng.* **2004**, *82*, 655–666.
- (7) Zhu, D.; Herbert, B. E.; Schlautman, M. A.; Carraway, E. R.; Hur, J. *J. Environ. Qual.* **2004**, *33*, 1322–1330.
- (8) White, C. E.; Provis, J. L.; Riley, D. P.; Kearley, G. J.; van Deventer, J. S. J. *J. Phys. Chem. B* **2009**, *113*, 6756–6765.
- (9) Ugliengo, P.; Zicovich-Wilson, C. M.; Tosoni, S.; Civalleri, B. *J. Mater. Chem.* **2009**, *19*, 2564–2572.
- (10) Tunega, D.; Benco, L.; Haberhauer, G.; Gerzabek, M. H.; Lischka, H. *J. Phys. Chem. B* **2002**, *106*, 11515–11525.
- (11) Michalkova, A.; Tunega, D.; Nagy, L. T. *J. Mol. Struct.: THEOCHEM* **2002**, *581*, 37–49.
- (12) Castro, E. A. S.; Martins, J. B. L. *J. Comput.-Aided Mater.* **2005**, *12*, 121–129.
- (13) Sainz-Díaz, C. I.; Francisco-Márquez, M.; Vivier-Bunge, A. *Theor. Chem. Acc.* **2010**, *125*, 83–95.
- (14) Austen, K. F.; White, T. O. H.; Marmier, A.; Parker, S. C.; Artacho, E.; Dove, M. T. *J. Phys.: Condens. Matter* **2008**, *20*, 035215.
- (15) Tunega, D.; Haberhauer, G.; Gerzabek, M. H.; Lischka, H. *Soil Sci.* **2004**, *169*, 44–54.
- (16) Pelmenschikov, A.; Leszczynski, J. *J. Phys. Chem. B* **1999**, *103*, 6886–6890.
- (17) Gorb, L.; Lutchny, R.; Zub, Y.; Leszczynska, D.; Leszczynski, J. *J. Mol. Struct.: THEOCHEM* **2006**, *766*, 151–157.
- (18) Michalkova, A.; Gorb, L.; Ilchenko, M.; Zhikol, O. A.; Shishkin, O. V.; Leszczynski, J. *J. Phys. Chem. B* **2004**, *108*, 1918–2930.
- (19) Robinson, T. L.; Michalkova, A.; Gorb, L.; Leszczynski, J. *J. Mol. Struct.: THEOCHEM* **2007**, *844–845*, 48–58.
- (20) Johnson, E. R.; Mackie, I. D.; DiLabio, G. A. *J. Phys. Org. Chem.* **2009**, *22*, 1127–1135 and references therein.
- (21) Becke, A. D.; Johnson, E. R. *J. Chem. Phys.* **2007**, *127*, 154108.
- (22) Otero-de-la-Roza, A.; Johnson, E. R. *J. Chem. Phys.* **2012**, *136*, 174109.
- (23) Johnson, E. R.; Keinan, S.; Mori-Sánchez, P.; Contreras-García, J.; Cohen, A. J.; Yang, W. *J. Am. Chem. Soc.* **2010**, *132*, 6498–6506.
- (24) Contreras-García, J.; Johnson, E. R.; Keinan, S.; Chaudret, R.; Piquemal, J.-P.; Beratan, D. N.; Yang, W. *J. Chem. Theory Comput.* **2011**, *7*, 625–632.
- (25) Otero-de-la-Roza, A.; Johnson, E. R. *Phys. Chem. Chem. Phys.* **2012**, *14*, 12165–12172.
- (26) Stone, A. J. *The Theory of Intermolecular Forces*; Clarendon Press: Oxford, 1996.
- (27) Hirshfeld, F. L. *Theor. Chim. Acta* **1977**, *44*, 129–138.
- (28) Becke, A. D.; Johnson, E. R. *J. Chem. Phys.* **2007**, *127*, 124108.
- (29) Kannemann, F. O.; Becke, A. D. *J. Chem. Theory Comput.* **2009**, *5*, 719–727.
- (30) Becke, A. D.; Roussel, M. R. *Phys. Rev. A* **1989**, *39*, 3761–3767.
- (31) Becke, A. D. *J. Chem. Phys.* **1986**, *85*, 7184–7187.
- (32) Perdew, J. P.; Burke, K.; Ernzerhof, M. *Phys. Rev. Lett.* **1996**, *77*, 3865–3868.

- (33) Otero-de-la-Roza, A.; Johnson, E. R. *J. Chem. Phys.* **2012**, *137*, 054103.
- (34) Blöchl, P. E. *Phys. Rev. B* **1994**, *50*, 17953–17959.
- (35) Giannozzi, P.; Baroni, S.; Bonini, N.; Calandra, M.; Car, R.; Cavazzoni, C.; Ceresoli, D.; Chiarotti, G. L.; Cococcioni, M.; Dabo, I. *J. Phys.: Condens. Matter* **2009**, *21*, 395502.
- (36) Becke, A. D. *J. Chem. Phys.* **1993**, *98*, 5648–5652.
- (37) Lee, C.; Yang, W.; Parr, R. G. *Phys. Rev. B* **1988**, *37*, 785–789.
- (38) Grimme, S. *J. Comput. Chem.* **2006**, *27*, 1787–1799.
- (39) Neder, R. B.; Burghammer, M.; Grasl, T.; Schulz, H.; Bram, A.; Fiedler, S. *Clay Clay Miner.* **1999**, *47*, 487–494.
- (40) Rimola, A.; Civalleri, B.; Ugliengo, P. *Phys. Chem. Chem. Phys.* **2010**, *12*, 6357–6366.
- (41) Tosoni, S.; Civalleri, B.; Ugliengo, P. *J. Phys. Chem. C* **2010**, *114*, 19984–19992.
- (42) Førland, G. M. *J. Colloid Interface Sci.* **2001**, *242*, 477–479.
- (43) Bader, R. F. W. *Atoms in Molecules. A Quantum Theory*; Oxford University Press: Oxford, 1990.
- (44) Otero-de-la Roza, A.; Blanco, M. A.; Martín Pendás, A.; Luaña, V. *Comput. Phys. Commun.* **2009**, *180*, 157–166.
- (45) Angove, M. J.; Fernandes, M. B.; Ikhsan, J. J. *Colloid Interface Sci.* **2002**, *247*, 282–289.
- (46) Elektorowicz, M.; El-Sadi, H.; Lin, J.; Ayadat, T. *J. Colloid Interface Sci.* **2007**, *309*, 445–452.
- (47) Soteras, I.; Orozco, M.; Luque, F. J. *Phys. Chem. Chem. Phys.* **2008**, *10*, 2616–2624.
- (48) Desiraju, D. R. *Acc. Chem. Res.* **1991**, *24*, 290–296.
- (49) Steiner, T. *Chem. Commun.* **1997**, *8*, 727–734.